Algorithm Theoretical Basis Document
Sea Ice Products

Thorsten Markus and Donald J. Cavalieri
Hydrospheric and Biospheric Sciences Laboratory
NASA Goddard Space Flight Center
Greenbelt, MD 20771

Josefino Comiso
NASA Goddard Space Flight Center
Greenbelt, MD 20771

July, 2012

1. Overview

The AMSR-E sea ice standard level 3 products include sea ice concentration, snow depth on sea ice, and sea ice drift. The AMSR-E standard sea ice concentration product is generated using the enhanced NASA Team (NT2) algorithm described by Markus and Cavalieri (2000, 2009), the snow depth is produced from the algorithm described by Markus and Cavalieri (1998) for both hemispheres, but excluding the Arctic perennial ice regions, and the sea ice drift is produced from an algorithm described by Liu and Cavalieri (1998). Additionally, the difference between the AMSR-E Bootstrap (ABA) (see ATBD by Comiso below) and the NT2 retrieved concentrations (ABA-NT2) are archived. These products together with AMSR-E calibrated brightness temperatures (TBs) are mapped to the same polar stereographic projection used for SSM/I data to provide the research community consistency and continuity with the existing 32-year Nimbus 7 SMMR and DMSP SSM/I sea ice concentration products. The TB grid resolutions are as follows: (a) TBs for all AMSR-E channels: 25-km, (b) TBs for the 18, 23, 36, and 89 GHz channels: 12.5-km, (c) TBs for the 89 GHz channels: 6.25-km. All of these TB products are stored as a composite of (i) daily-averaged ascending orbits only, (ii) daily-averaged descending orbits only, and (iii) all orbits creating a full daily average. Sea ice concentrations are produced at 12.5-km and 25-km resolutions and stored as a composite of daily-averaged ascending orbits, daily-averaged descending orbits, and all orbits for a full daily average, similar to the TB products. Snow depth on sea ice is produced as a 5-day average at a resolution of 12.5 km. Sea ice drift is also a five-day product computed at a resolution of 6.25-km, but mapped at a resolution of 100-km.

2. Sea Ice Concentration

2.1 Algorithm Theoretical Basis

The two ratios of brightness temperatures used in the original NASA Team algorithm (Cavalieri et al. 1984; Gloersen and Cavalieri 1986; Cavalieri et al. 1995) as well as in the NT2 approach are the polarization

$$PR(\nu) = [TB(\nu V) - TB(\nu)] / [TB(\nu V) + TB(\nu H)] \quad (1)$$

and the spectral gradient ratio

$$GR(\nu 1p\nu 2p) = TB(\nu 1p) - TB(\nu 2p)] / [TB(\nu 1p) + TB(\nu 2p)] \quad (2)$$

where TB is the brightness temperature at frequency ν for the polarized component p (vertical (V) or horizontal (H)).

Figure 1 (top) shows a typical scatterplot of PR(19) versus GR(37V19V) for September conditions in the Weddell Sea. The NT algorithm identifies two ice types which are associated with first-year and multiyear ice in the Arctic and ice types A and B in the Antarctic (as shown in Figure 1 (top)). The A-B line represents 100% ice concentration. The distance from the open water point (OW) to line A-B is a measure of the ice concentration. In this algorithm, the primary source of error is attributed to conditions in the surface layer such as surface glaze and layering (Comiso et al. 1997), which can significantly affect the horizontally polarized 19 GHz brightness temperature (Matzler et al. 1984) leading to increased PR(19) values and thus an underestimate of ice concentration. In the following discussion, we will refer to these effects as surface effects. In Figure 1 (top), pixels with significant surface effects tend to cluster as a cloud of points (labeled C) away from the 100% ice concentration line A-B resulting in an underestimate of ice concentration by the NT algorithm. The use of horizontally polarized channels makes it imperative to resolve a third ice type to overcome the difficulty of surface effects on the emissivity of the horizontally polarized component of the brightness temperature.

We make use of GR(89V19V) and GR(89H19H) to resolve the ambiguity between pixels with true low ice concentration and pixels with significant surface effects. A plot of these two ratios are found to form narrow clusters except for areas where surface effects decrease TB(19H) and consequently increase GR(89H19H) (Figure 1 (bottom)). Values of high GR(89V19V) and high GR(89H19H) are indicative of open water. The range of GR(89H19H) values is larger because of the greater dynamic range between ice and water for the horizontally polarized components. With increasing ice concentration, the two ratios have more similar values. The narrow cluster of pixels adjacent to the diagonal shown in Figure 1 (bottom) represents 100% ice concentration with different GR values corresponding to different ice types. When surface effects come into play, points deviate from this narrow cluster towards increased GR(89H19H) values (cloud of points to the right of the diagonal) while GR(89V19V) changes little or remains constant. This cloud of points labeled C in Figure 3 (bottom) also corresponds to the cluster of points labeled C in Figure 3 (top). The difference, therefore, between these two GRs (ΔGR) is used as a measure of the magnitude of surface effects. Based on this analysis we introduce a new ice type C which represents ice having significant surface effects. For computational reasons we rotate the axes in PR-GR space (Figure 1 (top)) by an angle φ so the A-B line is vertical. This makes the rotated PRs ($PR_R(19)$ and $PR_R(89)$) independent of ice types A and B (first-year and multiyear for the Arctic). The use of the 89 GHz data requires a correction for atmospheric effects. This is accomplished through an additional AMSR-E variable, PR(89).

The response of the brightness temperatures to different weather conditions is calculated using an atmospheric radiative transfer model (Kummerow 1993). Input data into the model are

the emissivities of first-year sea ice under winter conditions taken from Eppler et al. (1992) with modifications to achieve agreement between modeled and observed ratios. Atmospheric profiles used as another independent variable in the algorithm, having different cloud properties, specifically cloud base, cloud top, cloud liquid water are taken from Fraser et al. (1975) and average atmospheric temperatures and humidity profiles for summer and winter conditions are taken from Antarctic research stations. These atmospheric profiles are based on climatology and are assumed valid for both hemispheres.

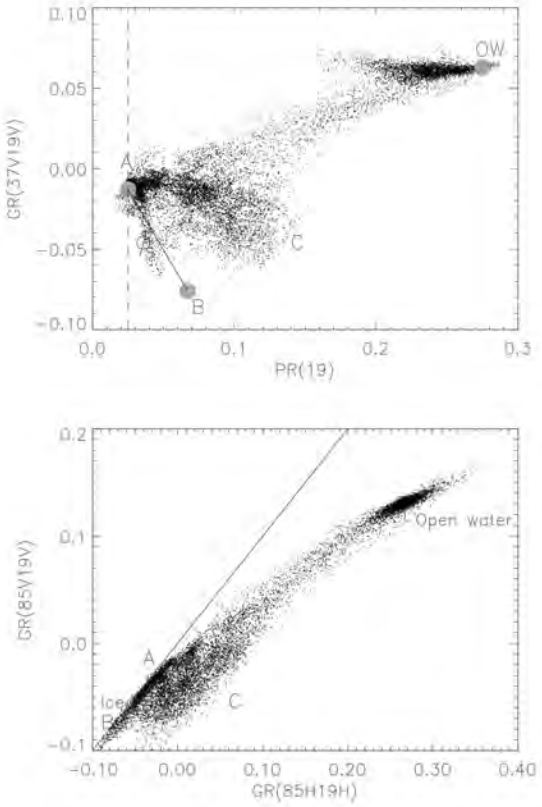

Figure 1: Top: GR(37V 19V) versus PR(19) for the Weddell Sea on September 15, 1992. The gray circles represent the tiepoints for the ice types A and B as well as for open water as used by the NT algorithm. Label C indicates pixels with significant surface effects. Φ is the angle between the y-axis and the A-B line. Bottom: GR(85V 19V) versus GR(85H19H). The ice types A and B are close to the diagonal. The amount of layering corresponds to the horizontal deviation from this line towards label C. Taken from Markus and Cavalieri [2000].

The plots of ΔGR versus PR_R (19) (Figure 2a) and ΔGR versus PR_R(89) (Figure 2b) illustrate the algorithm domain. The gray symbols indicate the tie-points with the different atmospheres for the three surface types (A, C, and OW). They also illustrate that the effect of weather is well modeled. For example, the cluster of open water values is mainly the result of changing atmospheric conditions. The modeled atmospheres adequately span the lengths of the OW clusters. A comparison of Figures B4a and B4b also shows how much more the 89 GHz data are affected by the atmosphere compared to the 19 GHz data.

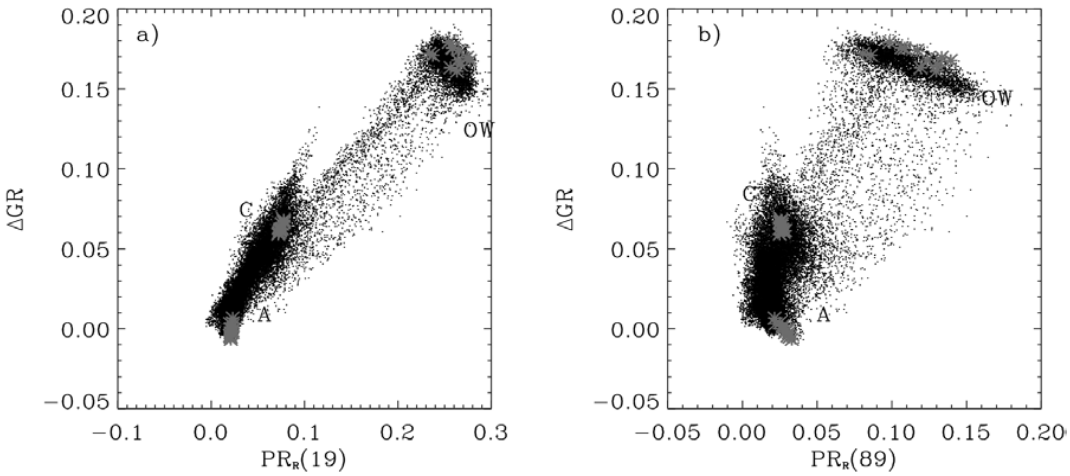

Figure 2 (a) ΔGR versus PR_R (19) and (b) ΔGR versus PR_R(89) for September 15, 2008. The gray symbols represent the NT2 tie

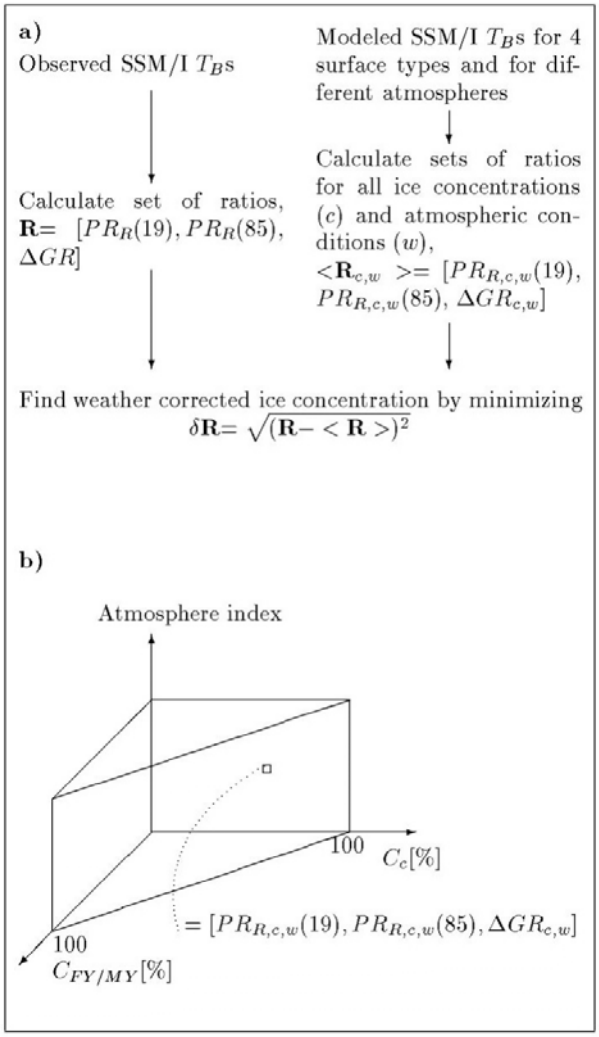

Figure 3. Flow diagram of the NT2 algorithm (from Markus and Dokken 2002).

We, then, calculate brightness temperatures for all possible ice concentration combinations in 1% increments and for each of those solutions calculate the ratios PR_R (19), PR_R (89), and ΔGR. This creates a prism in which each element contains a vector with the three ratios (Figure 3). For each AMSR-E pixel PR_R (19), PR_R (89), and ΔGR are calculated from the observed brightness temperatures. Next, we move through this prism comparing the observed three ratios with the modeled ones. The indices where the differences are smallest will determine the final ice concentration combination and weather index. The next section will provide detailed information about the implementation.

Because of the unique signature of new ice in the microwave range, we solve for new ice instead of ice type C for selected pixels. Using a GR(37V19V) threshold of –0.02 we either resolve ice type C (for pixels where GR(37V19V) is below this threshold) or thin ice (for pixels where GR(37V19V) is above this threshold). Areas of ice type C and thin ice are mutually exclusive because thin ice has little, if any, snow cover. A limitation, of course, is that we cannot resolve mixtures of thin ice and thicker ice with layering in its snow cover.

2.2 Implementation

2.2.1 Calculation of ice concentrations

In contrast to other operational sea ice concentration algorithms using daily averaged brightness temperatures as input, the AMSR-E NT2 concentrations are calculated from individual swath (Level 2) data from which daily maps are made by averaging these swath ice concentrations. Using swath brightness temperatures is particularly critical for the NT2 algorithm and its atmospheric correction. The atmospheric influence on the brightness temperatures is non linear and by using average brightness temperatures we would dilute the atmospheric signal. The ice concentration algorithm is implemented as follows:

1. Generate look-up tables: For each AMSR channel with frequency ν and polarization p calculate brightness temperature for each ice concentration-weather combination (using TBow, $TB_{A/FY}$, $TB_{C/thin}$ as given in the Appendix of Markus and Cavalieri (2009)):

$$TBca,cc,wx(\nu p) = (1 - C_A - C_C) \bullet TBow(\nu pWx) + C_A \bullet TB_{A/FY}(\nu pWx) + C_C \bullet TB_{C/thin}(\nu pWx) \quad (3)$$

where C_A refers to the ice type A/B concentration (FY/MY for Arctic), C_C to ice type C concentration, and Wx to the weather index. Ice concentrations are between 0 and 100 in 1% increments, weather indices are between 1 and 12 corresponding to the tables in the Appendix of Markus and Cavalieri (2009).

2. From these TBs calculate ratios creating the look-up tables, e.g. LUT $_{PR19(CA,CC,Wx)}$ etc.:

$$LUT_{PR19(CA,CC,Wx)} = [TBca,cc,wx(37V) - TBca,cc,wx(19V)] \times \sin\varphi_{19} / [TBca,cc,wx(37V) + TBca,cc,wx(19V)] + [TBca,cc,wx(19V) - TBca,cc,wx(19H)] \times \cos\varphi_{19}/$$

$$[TBca,cc,wx(19V) + TBca,cc,wx(19H)] \quad (4)$$

$$LUT_{PR89(ca,\ cc,wx)} = [TBca,cc,wx(37V) - TBca,cc,wx(19V)] \times \sin\varphi_{89}$$
$$TBca,cc,wx(37V) + TBca,cc,wx(19V)$$
$$+$$
$$[TBca,cc,wx(89V) - TBca,cc,wx(89H)] \times \cos\varphi_{89}/$$
$$[TBca,cc,wx(89V) + TBca,cc,wx(89H)] \quad (5)$$

If GR(37V19V) < -0.02 we solve for ice type C using ΔGR as our third variable, i.e.,

$$LUT_{dGR(ca,\ cc,wx)} = [TBca,cc,wx(89H) - TBca,cc,wx(19H)]/$$
$$[TBca,cc,wx(89H) + TBca,cc,wx(19H)]$$
$$-$$
$$[TBca,cc,wx(89V) - TBca,cc,wx(19V)]/$$
$$[TBca,cc,wx(89V) + TBca,cc,wx(19V)] \quad (6)$$

Whereas for pixels where GR(37V19V) > -0.02 we solve for thin ice using the standard GR(37V19V) as suggested by Cavalieri (1994), i.e.,

$$LUT_{dGR(ca,\ cc,wx)} = [TBca,cc,wx(37V) - TBca,cc,wx(19V)]/$$
$$[TBca,cc,wx(37V) + TBca,cc,wx(19V)] \quad (7)$$

Each of these arrays has the dimensions of 101 °— 101 °— 12 where, of course, the total ice concentration (ca + cc) cannot exceed 100.

3. For each pixel i we have the actual measured AMSR-E brightness temperatures (TBi(νp))

4. Calculate same ratios from these brightness temperatures as in step 2 (PRi(19), etc.).

5. Compare these observed ratios with each of the ratios in the look-up tables looping through all ice concentration-weather combinations, i.e.,

$$\delta = (PRi(19) - LUT_{PR19(ca,\ cc,wx)})^2 + (PRi(89) - LUT_{PR89(ca,\ cc,wx)})^2 + (\Delta GRi - LUT_{dGR(ca,\ cc,wx)})^2 \quad (8)$$

6. The indices ca, cc, wx where δ is minimal determine the ice concentration (and weather index), i.e.:

$$C_T = C_{A\min\delta} + C_{C\min\delta} \quad (9)$$

2.2.2 Land Spillover Correction

Although a land mask is applied to the ice concentration maps, land spillover still leads to erroneous ice concentrations along the coast lines adjacent to open water. This makes operational usage of these maps cumbersome. Therefore, we apply a land spillover correction scheme on the maps. The difficulty is to delete all clearly erroneous ice concentration while at the same time preserving actual ice concentrations, as for example, along the margins of coastal polynyas. We apply a five step procedure.

1. Classify all pixels of the polar-stereographic grid with respect to the distance to coast. Ocean pixels directly along the coast are classified by 1, whereas pixels farther away are 2 and 3. Open ocean pixels are zero. Land pixels directly along the coast are classified as 4 and pixels farther away have increasing values.

2. All pixels with classes 1 or 2 will be assessed for erroneous sea ice concentrations due to land spillover by analyzing the 7 by 7 pixel neighborhood. The area of the neighborhood (7 pixels or 87.5 km) needs to be greater than the AMSR-E antenna pattern. Pixels with values of 3 and 0 will not be changed.

3. Check whether all class 3 pixels in 7 pixel neighborhood are open water (if so, set ice concentration to 0).

4. Calculate an average sea ice concentration for the 7 by 7 pixel box assuming all ocean pixels have zero ice concentration and all land pixels have an ice concentration of 90%. This approximates a theoretical concentration caused by land spillover only.

5. If the AMSR-E ice concentration is less than or equal to this value, set pixel at center of box to open water.

Figure 4 shows an example ice concentration with and without the land spillover correction.

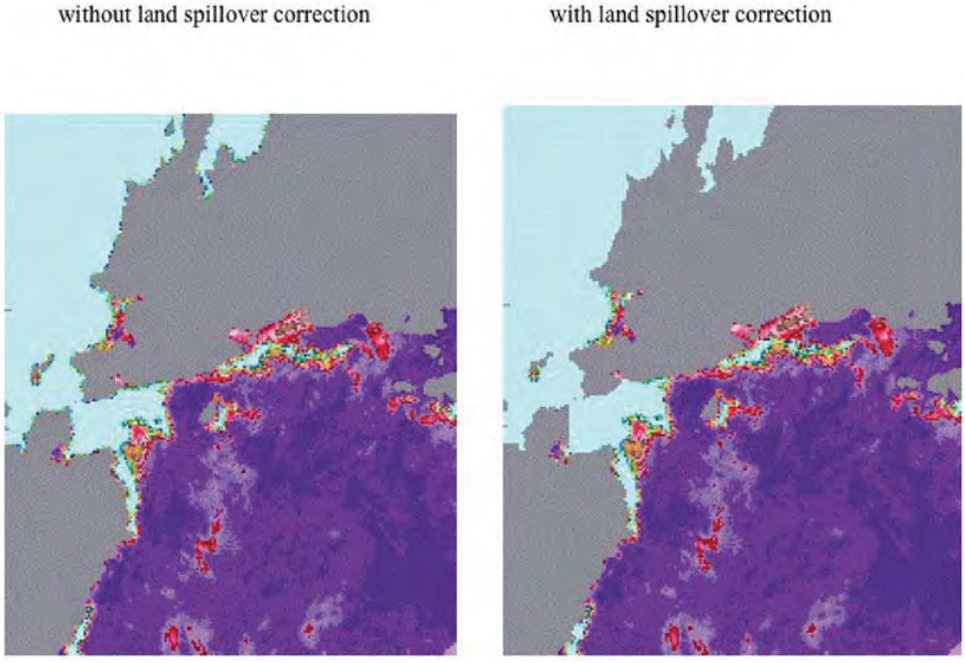

Figure 4 Map of ice concentration with and without land spillover correction

2.2.3 Reduction of Atmospheric Effects

The NT2 algorithm has an atmospheric correction scheme as an inherent part of the algorithm. It provides weather-corrected sea ice concentrations through the utilization of a forward atmospheric radiative transfer (RT) model. However, to eliminate remaining severe

weather effects over open ocean, two weather filters based on the spectral gradient ratio are implemented using threshold values similar to those used by the NT algorithm (Gloersen and Cavalieri 1986; Cavalieri et al. 1995). However, the advantage of the RT atmospheric correction is that not only are spurious ice concentrations over the open ocean removed, but atmospheric corrections are applied to ice covered portions of the ocean.

Figure 5 shows AMSR-E sea ice concentration maps for the Sea of Okhotsk. Figure 5a shows the ice concentration map if PR_R (19), PR_R (89), and ΔGR are used without any weather correction. Figure 5b shows the ice concentration map with the NT2 weather correction. The differences between Figure 5a and 5b are shown in Figure 5d and illustrate the effect of the weather correction not only over the open ocean, but also over the sea ice. More severe weather effects over the open ocean (for example, in the bottom right corner) are finally removed by the NT weather filters (Figure 5c). The threshold for the GR(37V19V) NT weather filter (Gloersen and Cavalieri 1986) is 0.05, where the threshold for the GR(22V19V) NT weather filter (Cavalieri et al. 1995) is 0.045. If the respective GR values exceed these thresholds, the sea ice concentrations are set to zero. Figure 5e shows the difference in ice concentrations between the retrievals using only the NT2 weather correction and the retrievals using both the NT2 correction and the NT filters. A slight change along the ice edge is observed.

Even with both the atmospheric correction scheme and the GR filters, we still had problems with residual weather contamination particularly at low latitudes. A filter based on monthly climatological sea surface temperatures (SSTs) from the National Oceanic and Atmospheric Administration (NOAA) ocean atlas, used earlier by Cavalieri et al. (1999), was employed to eliminate these low-latitude spurious ice concentrations. In the Northern Hemisphere, any pixel where the monthly SST is greater than 278 K, the ice concentration is set to zero throughout the month; whereas in the Southern Hemisphere, wherever the monthly SST is greater than 275 K, the ice concentration is set to zero throughout the month. The higher SST threshold value in the Northern Hemisphere is needed because the 275 K isotherm used in the Southern Hemisphere is too close to the ice edge in the north. The closest distance the threshold isotherms are to the ice edge is more than 400 km (Cavalieri et al. 1999).

In summary, the order of processing is as follows:

1. Calculate sea ice concentrations with atmospheric correction.
2. Apply GR filters.
3. Apply SST mask.
4. Apply land spillover correction.

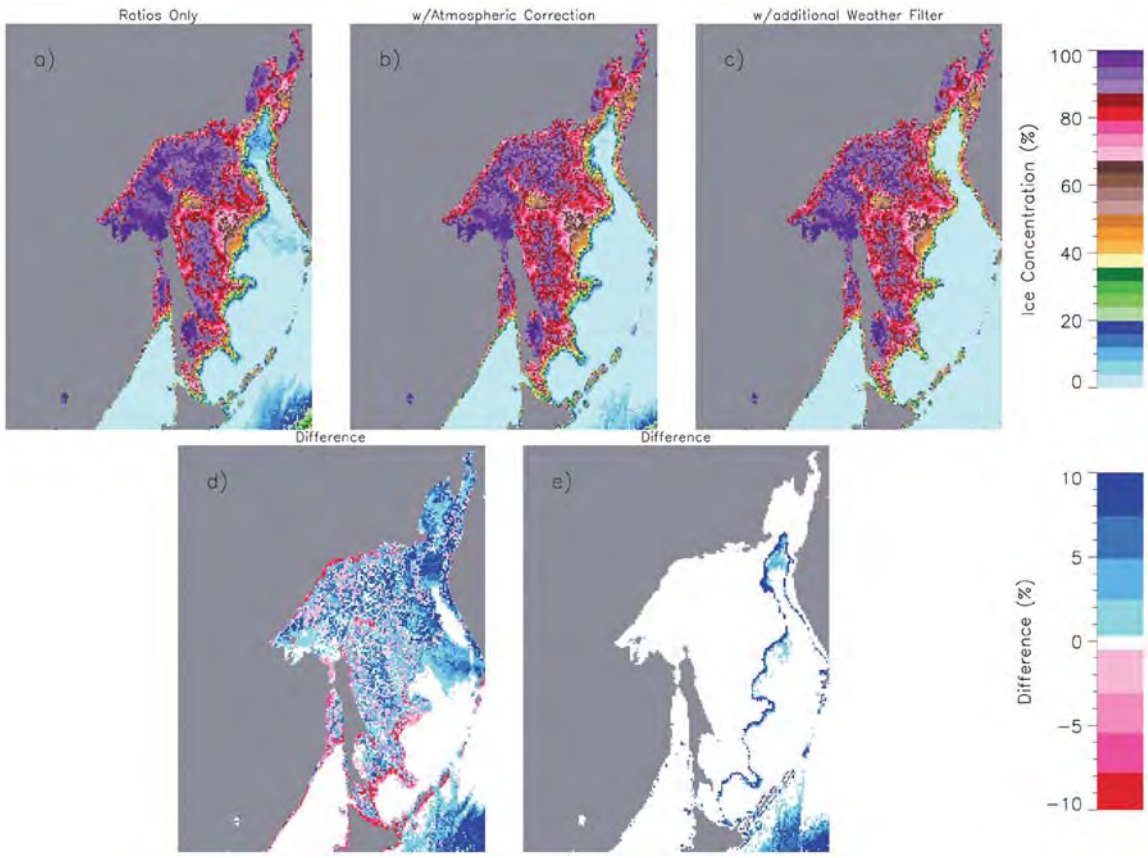

Figure 5. AMSR-E sea ice concentrations for March 1, 2007. (a) Ice concentrations calculated using PR_R (19), PR_R (89), and ΔGR without applying an atmospheric correction; (b) ice concentration with atmospheric correction; (c) final ice concentration with additional clean-up over the open ocean by applying the standard NASA Team GR weather filters; (d) difference between (a) and (b); (e) difference between (b) and (c). Differences greater than 10% have been truncated for the erroneous sea ice concentrations in the lower right corner.

3. Snow Depth on Sea Ice

3.1 Algorithm Theoretical Basis

The AMSR-E snow-depth-on-sea-ice algorithm was developed using DMSP SSM/I data (Markus and Cavalieri 1998) to estimate snow depth on sea ice from space. The snow depth on sea ice is calculated using the spectral gradient ratio of the 18.7 GHz and 37 GHz vertical polarization channels,

$$h_s = a_1 + a_2\,GRV(ice) \qquad (10)$$

where h_s is the snow depth in meters, and a_1=2.9 and a_2=-782 are coefficients derived from the linear regression of *in situ* snow depth measurements on microwave data. GRV(ice) is the spectral gradient ratio corrected for the sea ice concentration, C, as follows

$$GRV(ice) = [T_B(37V)-T_B(19V)-k_1(1-C)] / [T_B(37V)+T_B(19V)-k_2(1-C)] \quad (11)$$

with $k_1=T_{BO}(37V)-T_{BO}(19V)$ and $k_2=T_{BO}(37V)+T_{BO}(19V)$. The open water brightness temperatures, T_{BO}, are average values from open ocean areas and are used as constants. The principal idea of the algorithm is similar to the AMSR-E snow-on-land algorithm (Kelly et al. 2003) utilizing the assumptions that scattering increases with increasing snow depth and that the scattering efficiency is greater at 37 GHz than at 19 GHz. For snow-free sea ice, the gradient ratio is close to zero and it becomes more and more negative as the snow depth (and grain size) increases. The correlation of regional *in situ* snow depth distributions and satellite-derived snow depth distributions is 0.81 (Figure 6). The upper limit for snow depth retrievals is 50 cm which is a result of the limited penetration depth a 19 and 37 GHz.

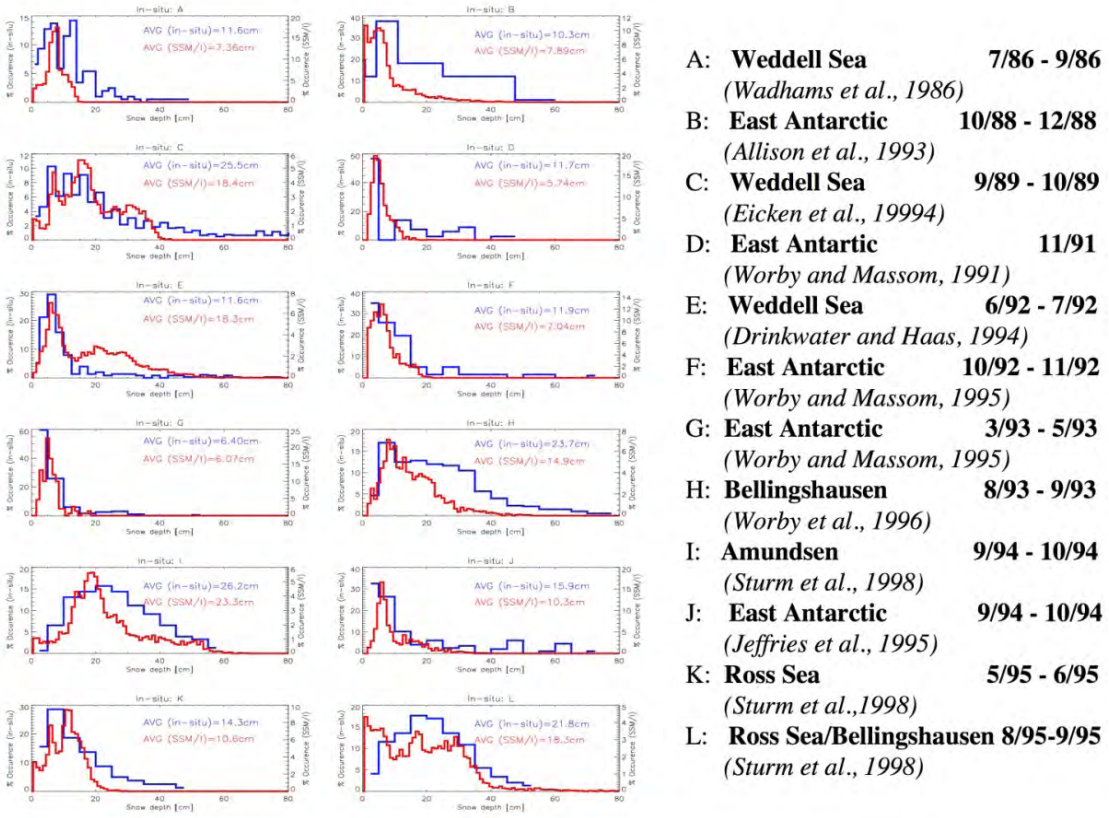

Figure 6: Comparison of in-situ and SSM/I-derived snow depth distributions [from Markus and Cavalieri 1998].

3.2 Implementation

The algorithm is applicable to dry snow conditions only. At the onset of melt, the emissivity of both the 19 GHz and the 37 GHz channels approach unity (that of a blackbody) and the gradient ratio approaches zero initially before becoming positive. Thus, snow depth is indeterminate under wet snow conditions. Snow, which is wet during the day, frequently refreezes during the night. This refreezing results in very large grain sizes (Colbeck 1982) which leads to a reduced emissivity at 37 GHz relative to 19 GHz thereby decreasing GRV(ice) and

thus leads to an overestimate of snow depth. These thaw-freeze events, therefore, cause large temporal variations in the snow depth retrievals. This temporal information is used in the algorithm to flag the snow depths as unretrievable from those periods with large fluctuations.

As grain size *in situ* measurements are even less frequently collected than snow depth measurements, the influence of grain size variations could not be incorporated into the algorithm. Because of the uncertainties in grain size and density variations as well as sporadic weather effects, AMSR-E snow depth products will be 5-day averages similar to the snow-on-land product.

Snow depths are retrieved for the entire Southern Ocean, but only for the seasonal sea ice zones in the Arctic, because the microwave signature of snow is very similar to the multiyear ice signature so that snow depth on multiyear ice cannot be retrieved unambiguously. To this end, we use a dynamic multiyear ice mask based on a threshold in GR which evolves on a day-to-day basis starting from October 1 of each year until the onset of melt.

4. Sea Ice Drift

4.1 Algorithm Theoretical Basis

The sea ice drift algorithm applies a wavelet transform to the 89 GHz Horizontal (H) channel of the AMSR-E L3 6.25 km brightness temperature map gridded at a resolution of 6.25 km for ice feature detection. These ice features are tracked from day-to-day providing sea ice speed and direction at grid points mapped every 100 km. The algorithm, originally developed at Goddard Space Flight Center (GSFC) for use with DMSP SSM/I imagery, is described by Liu and Cavalieri (1998). The algorithm provides sea ice drift for 5-day periods for both the Arctic and the Antarctic.

The following has been adapted from Liu and Cavalieri (1998) and describes the derivation techniques:

The wavelet transforms of satellite images can be used for near-real-time quick-look analyses of satellite data for feature detection, for data reduction using a binary image, and image enhancement by edge linking. In general, the continuous wavelet transform, Ws (a, b), of a function, s (r), where r = (x, y), is expressed in terms of the complex valued wavelet function, w(r), as follows:

$$Ws(a,\mathbf{b}) = (1/\sqrt{a}) \int s(\mathbf{r}) w^*(\mathbf{r}-\mathbf{b}/a) \mathrm{d}\mathbf{r} \qquad (12)$$

in which the wavelet function is dilated by a factor a, and shifted by b. The function w(r) is the basic wavelet (Combes et al. 1989). The superscript * indicates complex conjugate. For data analysis, the wavelets frequently used are: a Gaussian modulated sine and cosine wave packet, known as the Morlet wavelet; and the second derivative of a Gaussian, often referred to as the Mexican hat.

4.2 Implementation

To determine drift vectors only over sea ice, not open water, a sea ice mask is used within the sea ice drift algorithm code. Derived from the 18 GHz and 37 GHz Vertical (V) channels of the AMSR-E L3 12.5 km brightness temperature product, the mask approximates sea ice coverage in order to mask out unused vector points.

- Closed contours (those with no other features crossing them, called zero-crossing contours) correspond to the boundary of ice features. Yet these zero-crossing contours may contain many different ice features. To associate a single closed contour with an isolated ice feature, a five percent threshold above the minimum of the wavelet transform is applied as the contour value.
- Next, each closed contour is framed in a rectangular window with its four sides just tangent to the four extreme locations of the closed contour. Each window at a given starting date is used as a template to be matched. The template window is not fixed in size, but is determined by the ice feature at a particular location.
- With the template defined, the templates are then matched with the results from the wavelet transform of the AMSR-E image four days later. Because of the 6.25 km resolution of the AMSR-E image, the displacement of the ice feature may move just a pixel or two in several days. Thus, the domain of the template matching can be restricted to an area with a few pixels (such as 20 pixels) larger than the template window. The matching is done by shifting the template over each pixel in the domain.
- For each location, the absolute values of the differences between the shifted template values and the target values are then summed.
- The sequence of the summation values is then used as a metric of the degree of match of the ice feature. Its minimum indicates a possible match of two displaced ice features. Once the shapes have been matched, the velocity vector can be easily estimated from dividing the relative displacement over a time interval of four days.

Note that the method of template matching outlined above uses a template window determined by the threshold of the wavelet transform of AMSR-E images. This method of template matching of ice features is very efficient, as the only computations involved are logical operations, addition, and subtraction. Furthermore, it is only necessary to match the template pattern to a limited number of target patterns generated by the results of the wavelet transform, not to every location in the image as with classical template matching. Note also that although template correlation is applied here only to find the translation of the target pattern with respect to the template pattern, it can be extended to find the rotation of the target pattern by incremental rotation of the target pattern in direction and then matching the extent of their agreement (Liu and Cavalieri 1998).

In summary, once a sea ice feature is identified, it is tracked from day-to-day over 4 days. The total displacement over this period then is used to calculate the 5-day sea ice drift (speed and direction). The sea ice speed is given in centimeters per second (cm/s) and direction is given in radians from the horizontal axis of the grid counterclockwise.

Zhao and Liu (2007) have compared the AMSR-E sea ice drift with Arctic Ocean buoy data and obtained an RMS error of 3.1 cm/s for the AMSR-E sea ice speed and an RMS error of 26.4 degrees for the AMSR-E sea ice direction.

AMSR-E Bootstrap Sea Ice Algorithm

Josefino Comiso
NASA Goddard Space Flight Center
Greenbelt, MD 20771

1. Introduction

Historical records of the global sea ice cover, as derived from satellite passive microwave data, have provided some of the most important climate change signals that may be associated with anthropogenic greenhouse gases. One of the most revealing results from satellite microwave data is the large rate of decline of the Arctic perennial ice extent which is currently at -13.5 % per decade and its thick multiyear ice component at -15% per decade (Comiso 2012). In September 2007, the perennial ice cover was not only the record low but also 40% lower than the average value since 1978, and 27% lower than the previous low value in 2005 (Comiso et al. 2008). A slight recovery followed but in September 2011, the perennial ice cover was about as low as in 2007. This phenomenon has been recognized as one of the most intriguing climate change signals coming from the Arctic region. The anomalously high sea surface temperature during the period and the strong possibility of having an ice free ocean in the Arctic in the summer in the near future has been reported (Shibata et al. 2010; Lindsay and Zhang 2005; Wang and Overland 2009). The potential impact of such an event on the ecology, environment, navigation and mineral exploration has been the subject of many studies (e.g., Bhatt et al. 2010). On the other hand, similarly intriguing is that the sea ice cover in the Antarctic region has been changing as well but in the opposite direction (Zwally et al. 2002; Comiso et al. 2009). Such positive trend, which is now about 2% per decade, has been postulated to be in part caused by the deepening of the lows in West Antarctica associated with the Ozone hole that in turn have caused stronger winds off the Ross ice shelf and hence more ice production in the Ross Sea region (Turner et al., 2009). Enhanced ice production in the Ross Sea has been confirmed (Comiso et al. 2009) but other studies indicate that other processes not linked to stratospheric ozone depletion must be invoked to explain the observed increase in the Antarctic extent since 1979 (Sigmond and Fyfe 2010). Because of many important issues associated with the aforementioned changes, accurate characterization of the global sea ice cover more than ever needed. Such product should also be consistent with historical data to enable meaningful trend and variability studies.

2. Algorithm Overview

Monitoring the sea ice cover with satellite passive microwave data has had a long history, starting with the Nimbus-5 Electrically Scanning Microwave Radiometer (ESMR) launched in December 1972, continuing with the Nimbus-7 Scanning Multichannel Microwave Radiometer (SMMR), launched in October 1978, and then with the series of DMSP Special Scanning Microwave Imagers (SSM/I) the first of which was launched in July 1987. The data from these

sensors have provided the continuous and consistently derived sea ice concentration data from 1978 up to the present (Comiso and Nishio 2008). The data, however, are not without any shortcomings among which are the relatively coarse resolution, significant radiometer noise and antenna side lobes. The launch of the Japanese Advanced Microwave Scanning Radiometer (AMSR-E) on board the EOS/Aqua satellite in May 2002 and a similar version (AMSR) on board ADEOS-2 satellite in December 2002 provided a new era in the remote sensing of sea ice. The new system has a much better resolution, wider spectral range and larger swath width than previously available data. For example, the resolution of the 37 GHz channel for SSM/I is 30 x 38 km while that of AMSR-E at approximately the same frequency is 10.3 x 13.7 km. The higher resolution has enabled more accurate identification of the ice edge and improved characterization of the ice cover in the inner zones (Comiso and Nishio 2008). It also enabled assessments of snow cover and surface ice temperature as well as improved estimates of drift velocities of the ice floes (Markus and Cavalieri 1998; Comiso et al. 2003; Yaguchi and Cho 2009). Further improvements in accuracy are expected with the launch of the GCOMW1/AMSR2 sensor because of significantly higher resolution of the latter (i.e., 7x12 km for AMSR2 compared to 10x14 for AMSR-E and 30x38 km for SSM/I at 37 GHz).

The Bootstrap Algorithm has had a long history and has been used to generate sea ice data from 1978 to the present (Comiso 2010). It makes use of three frequency channels (i.e., 18.7 at vertical polarization, 36.5 GHz at both vertical and horizontal polarization and 22 GHz at vertical resolution) that are available continuously from SMMR, through SSM/I and to AMSR-E. The algorithm is thus ideally suited for generating long term and consistent data set needed for detailed studies of the variability and trends in the sea ice cover. The launched of AMSR2 aboard the GCOM-W satellite in May 2012 is a most welcomed development, especially with the demise of AMSR-E in 2010. Among the objectives of the JAXA/Global Change Observation Mission (GCOM) and NASA's Earth Observing System is to understand global climate change through the use of long-term satellite observing systems. It is important that the sea ice data set that had been enhanced by AMSR-E will continue with AMSR2, especially during the current climatic period when the sea ice cover is undergoing not just large seasonal and interannual variability but also rapid declines in the Arctic and some increases in the Antarctic.

3. Theoretical Description

The conversion of digital satellite data to sea ice parameters requires a knowledge of some basic geophysical parameters, among which are surface temperature and the microwave emissivity of the surface at the different frequency and polarization channels of the sensor. In addition, atmospheric effects that vary from one location to another and from one day to the next have to be taken into account. The brightness temperature, (T_B), recorded by satellite passive microwave sensors at a given wavelength can be estimated using the basic radiative transfer equation given by

$$T_B = \varepsilon T_S e^{-\tau} + \int_0^{\tau} T(z)\, \varsigma(z) e^{-\tau + \tau'(z)} d\tau'(z) + (1 - \varepsilon)\kappa e^{-\tau} \int_0^{\tau} T(z)\, \varsigma(z) e^{-\tau'(z)} d\tau'(z) \quad (13)$$

where ε is the emissivity of the surface, T_S is the physical temperature of the surface, τ'(z) and τ are the atmospheric opacities from the surface to a height z and from the surface to the satellite height, respectively, κ is an estimate of the diffusiveness of the surface reflection, and T(z) and ς (z) are the temperature and the emittance at z. In equation 13, the first term represents radiation directly from the earth's surface, which is the dominant contribution for measurements at microwave frequencies. The second term represents satellite observed upwelling radiation that emanates directly from the atmosphere, while the third term represents downwelling radiation from the atmosphere that has been reflected by the surface before it reaches the satellite detector. A fourth term that takes into account the reflected contribution of radiation from free space (i.e., the cosmological 2.7 K contribution from the Big Bang), which is an additive contribution, is usually negligible and not included in equation 10. This radiative transfer equation provides the means to transform the top of the atmosphere brightness temperature as measured directly by satellite sensors to surface brightness temperature needed to obtain the geophysical surface parameter. The brightness temperature of the surface of interest is equal to εT_S which is part of the first term in equation 10. The atmospheric parameters and also surface emissivity as required by the equation changes spatially and temporally and are unfortunately not known on a real time basis and hence the need to develop an alternative procedure. The Bootstrap Algorithm is designed to take the atmospheric contribution into account in an indirect manner through a technique based on the utilization and analysis of real time data. With the Bootstrap Algorithm, a multichannel scheme was developed in which the patterns in the distribution of data points and clustering of these points in a multi-dimensional space are used to indirectly infer emissivity and at the same time, take into account spatial variations in surface temperature and atmospheric effects.

3.1 Tie-Point and Threshold Optimization

The basic assumption of the Bootstrap Algorithm for ice concentration is that within the ice pack, the surface is covered by either sea ice or ice free (liquid) water. The brightness temperature recorded by the satellite passive microwave sensor within each field-of-view is thus a contribution of radiation from ice covered surfaces and from ice-free surfaces. The brightness temperature, T_B, as measured by AMSR-2 is thus assumed to be a linear combination of the two surfaces as expressed by the following mixing formulation:

$$T_B = T_I C_I + T_O C_O \quad (14)$$

where T_I is the brightness temperature of 100% ice covered areas and T_O is the corresponding value of 100% open water, while C_I and C_O are the percentage concentrations for sea ice and open (ice free) water respectively. Using the relationship, $C_O + C_I = 1$, and assuming that the

observational area is covered only by either ice or water, equation 15 can be solved explicitly for C_I and the result is as follows

$$C_i = (T_b - T_o)/T_i - T_o \quad (15)$$

Equation 15 is the fundamental formula that has been used by all sea ice concentration algorithms. It is a relatively simple formula but not so easy to implement. The big challenge has been how to obtain good estimates of the surface values of T_B, T_O and T_I which are all functions of emissivity (ε), surface temperature (T_S), and atmospheric opacity. In principle, the equation is independent of sensor resolution and should provide similar results regardless of resolution. But there are exceptions especially near boundaries of ice and water and in areas where the contrast in the emissivity of sea ice and water are not strong enough to enable a good discrimination of the two surfaces. In such areas, there could be a smearing of data as is normally the case at the marginal ice zone in part due to antenna side lobes. In general, the higher the resolution, the better the chances in getting the correct location of the ice edge and in getting accurate characterizations of the marginal ice zones.

An ideal algorithm for retrieving the ice concentration would be the one that calculates accurately the surface values of the parameters T_B, T_O and T_I in equation 15 at each field-of-view (or data element) of satellite observation. This means that all three parameters have to be corrected for atmospheric effects at each measurement. The usual technique is to utilize a radiative transfer model which makes use as input, atmospheric profile parameters to take into account the effect of spatially and temporally changing opacity τ of the atmosphere as indicated in equation 13. Such atmospheric contributions can be as large as 20% of the satellite observed signal and are therefore important to take into account.

Earlier algorithms were based on radiative transfer models that used atmospheric profiles taken from averages derived from radiosonde data at some Arctic regions (Svendsen et al. 1987; Swift et al. 1985). These algorithms were reasonably successful in regions where and time periods when such radiosonde data are acquired and used for atmospheric corrections. Generally, however, there are problems when they were used as a global algorithm because of large spatial and temporal variability of atmospheric and surface conditions. The algorithms that are currently more frequently utilized are those that take advantage of the multichannel capability of the satellite data in obtaining the required input parameters in equation 16 as described in Comiso et al. (2003). Two of these algorithms are the Bootstrap Algorithm and the Nimbus-7 Team Algorithm (now called the NASA team algorithm), both developed at the NASA Goddard Space Flight Center (Cavalieri et al. 1984; Comiso 1986). The original Team Algorithm used three tie points: two for the two general ice types (i.e., first year and multiyear ice) and one for open water, and employs polarization and gradient ratios to minimize the effect of varying surface temperatures. The different techniques for accounting for spatial changes in ice temperature and emissivity and the use of different sets of channels yielded different results

between the Team Algorithm and the Bootstrap Algorithm (Comiso et al. 1997; Comiso and Steffen 2001) in large areas of the polar regions. The different results were attributed to different sensitivity of the polarization ratios to surface effects, including ice and snow layering, as discussed in Matzler (1984). The original NASA Team Algorithm (now called NT) has been substantially revised to make use of the 89 GHz in combination with other channels and is currently called NT2 (Markus and Cavalieri 2000). With NT2, a radiative transfer model (e.g., Kumerow 1993) has to be used to correct for the high sensitivity of the 89 GHz data to atmospheric effects. It also requires some accounting on the large variations in the surface emissivity of sea ice at this frequency. The results from NT2 have been shown to be an improvement to that of NT and are in much better agreement with those of the Bootstrap Algorithm but there are still significant differences (Parkinson and Comiso 2008; Comiso and Parkinson 2008). Such differences are believed to be associated in part with the use of the 89 GHz data (in NT2) which at times could cause errors due to inadequate accounting of atmospheric and surface effects. The differences are also in part due to differences in resolution since the two algorithms uses different sets of frequency channels.

A schematic illustration of the distribution of data points in ice covered and open ocean region is shown in Figure 7 using data from two radiometer channels. Data points in consolidated ice regions where the ice concentrations are close to 100% usually form a linear cluster along a line near AD. Those in the open water areas would be along the line AW. The scheme for finding the two tie points for ice concentration is to utilize the line AD in Figure 7 as the reference for 100% ice and the data point O for 100% liquid (or open) water. Data points located between the line AD and O are interpreted as having ice concentrations between 0 and 100% in this scheme. Thus, given a data element at a hypothetical data point B in the plot measured by the satellite sensor, the ice concentration can be derived by first extending the line along OB until it intersects the line AD. The brightness temperature T_I at the intersection point, I, represents 100% ice for this particular ice type/surface while the brightness temperature T_O at O represents 0% ice. Using this tie-point values in equation 17, ice concentration can be calculated. This can be done for either channels (along the horizontal or the vertical), but when T_O and T_I are close or equal to each other, as can happen at 36 GHz (V) and higher frequencies, there is a singularity problem (i.e., if $T_O = T_I$). Thus, the ratio of OB to OI is usually used, as described in Comiso (1995), which provides the same value as the ratio of the numerator and denominator in equation 12. It should be noted that ice concentrations below a cut-off of about 10% are derived because the emissivities of ice and water are mainly impossible to discriminate at such values as discussed below.

The line AD is determined by the algorithm on a daily basis and inferred from a regression analysis of data points above the red dash line in Figure 7. The red dash line is determined such that most of the data points above it have near 100% sea ice concentration. A small positive value of a few Kelvins is added to the offset of the regression line to account for the known presence of open water (of about 2 % in the Arctic and 4% in the Antarctic) for much of the

consolidated ice regions. The estimate of the parameters of the line AD is critical to the accuracy of the ice concentration estimate. With AMSR2 data, the values of the offsets will be optimized such that the retrieved ice concentration values are as consistent as possible with those from validation data sets (e.g., high resolution satellite data or detailed ship or aircraft observations) and at the same time allows for variations in surface emissivity and atmospheric attenuation.

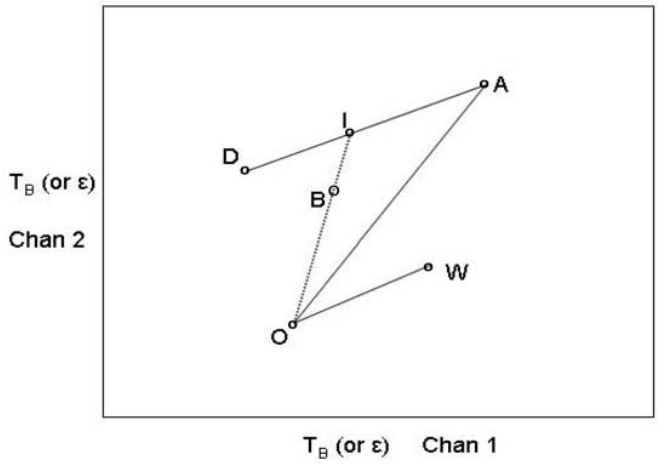

Figure 7. Schematics for the choice of tie-points in the Bootstrap Algorithm. Data points along AD are considered as having 100% ice concentration while those along OW have 0% ice concentration.

The criteria used for choosing the channels for the algorithm are: (a) they provide the geophysical parameter at the optimal resolution and accuracy; and (b) ancillary data are used only if absolutely necessary to improve accuracy. Thus, the set of 36.5 GHz channels (called HV36) is used because of reasonably good resolution and at the same time takes into account spatial variations in surface temperature and emissivity for accurate retrieval. With this set, the data in the consolidated ice regions form a linear cluster with a well defined slope for AD (when one polarization is plotted versus the other) the value of which is approximately equal to one. The values form a linear distribution because the wavelengths are the same and emissivity of ice is approximately the same for the two polarizations. Thus, they are affected by intermediary factors, like snow and the atmosphere, in much the same way. What makes it even more valuable is that the set is basically insensitive to spatial variations in temperature since the slope is approximately one and any change in the brightness temperature due to temperature as observed in one channel is approximately equal to that in the other channel. Thus the net effect of a changing temperature is to cause T_I to slide along the line AD and practically no impact on the accuracy in the retrieval of ice concentration.

The algorithm complements the use of the set of 36.5 GHz channels with another set using 18 (or 19) GHz at vertical polarization which we call the V1836 set. This other set provides the means to remove some ambiguities in the HV36 set since in this set of channels, the open ocean

data cluster (i.e., the line OW) is either along the line OA in Figure 7 or to the left of this line. Furthermore, the horizontal channel is more sensitive to layering and other surface effects than the vertical channel (Matzler et al. 1984) and in some ice covered areas, the data points fall below or to the right of the line AD. Both problems are resolved through the additional use of a set of channels that utilizes the 18 (or 19) GHz in combination with the 36.5 (or 37) GHz channel at vertical polarization (thereafter called the V1836 set) which provides an even easier discrimination and a good contrast between the emissivity of ice and water. The use of the V1836 set shows some sensitivity to variations in surface ice temperature but the associated error is relatively minor because sea ice is usually covered by snow which is a good insulator and the spatial variability of observed surface ice temperature is not much. The standard deviation of observed snow/ice interface temperatures has been about 2.5K.

3.2 Statistical Error Analysis

Figure 8 provides the means to evaluate how accurately the sea ice concentration can be derived from the HV36 set of channels. The data points are from winter data in the Northern Hemisphere and the distribution for consolidated ice (in blue) is indeed quite compact and the slope is close to 1. The accuracy in the estimate of C_I depends mainly on the accuracy in the estimate of T_I since it is known that T_I varies a lot more than T_O in the pack ice regions. The accuracy in the estimate of T_I is in turn dependent on how well AD represents 100% ice. The more well defined the linear cluster AD is, the more accurate the retrieval is going to be. To quantify how well defined the ice cluster AD is, the scatter plot is rotated such that the AD cluster is along the vertical as shown in orange in Figure 8a. The width of the cluster can then be quantified with a frequency histogram of the sum of data points along the vertical within each horizontal bin and the results are shown in Figure 8b. In the plot, the peak in the left represents the distribution of consolidated ice data points along an arbitrary horizontal axis that can be converted to ice concentration since the relative location of TO is also shown in the plot (approximately the highest data point to the right). After the conversion, the standard deviation of the ice peak is about 1.5 units which is estimated to be equivalent to less than 3% ice concentration. The actual uncertainty in the ice concentration associated with the variability of T_I would be even smaller since the consolidated ice data points include a fraction of open water within a relatively large footprint (which in this case is 25 by 25 km).

3.3 Systematic and Residual Errors

The aforementioned retrieval technique for ice concentration is appropriate only in ice covered oceans. Applying the same algorithm over land and open oceans would yield non-zero ice concentration values and hence the need for a land and liquid ocean masks. Such land and liquid masks are usually not perfect and would affect the accuracy of the retrieval of areas covered by sea ice. The land mask, that has been previously used were based on published boundaries of land areas. The published boundaries have been shown to be inaccurate in some

areas when compared with high resolution satellite data. This is in part because in the polar regions, the land/ocean boundaries are not permanent because of iceberg calving, glacial surging or retreat and ice melt. The land mask to be used for AMSR2 will be an enhanced version of the one currently used for AMSR-E and will be based on MODIS or higher resolution satellite data.

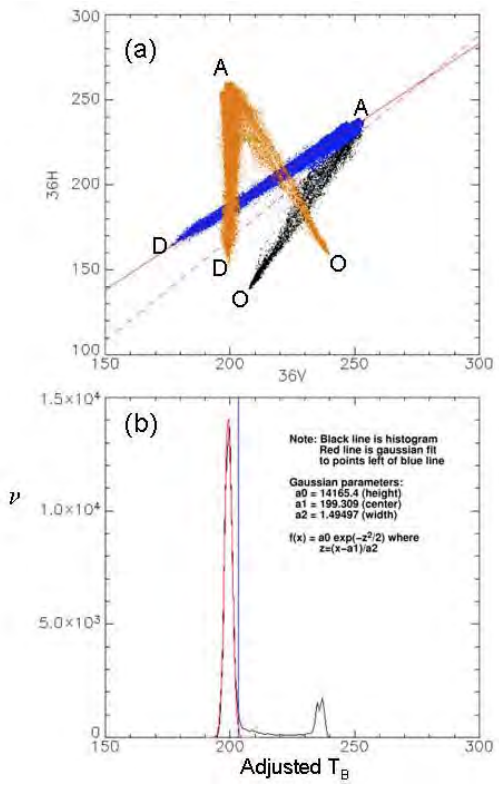

Figure 8. (a) Scatter plot of 36 GHz(V) versus 36 GHz(H) brightness temperatures with the ice cluster along AD shown as blue data points. Also shown is the same set of data points with data points rotated (in orange) such that the line AD cluster is along the vertical. (b) frequency distribution of rotated data points (orange) in (a). The standard deviation of the distribution for the ice curve (red line) is 1.5 $^{\circ}$K which is approximately 2% in ice concentration.

An open ocean mask has been developed by identifying the location of data points that correspond to such open oceans areas in the scatter plots of one channel versus another. Most of the data points in the open ocean can be isolated and identified readily using this procedure but there are significant number that are problematic. In particular, areas in the open ocean that are under the influence of inclement weather conditions can have signatures similar to those of ice covered ocean. We make use of a combination of 19, 22, and 36 GHz brightness temperatures (T_B) at vertical (V) and horizontal (H) polarizations to discriminate open ocean data from ice data during such unusual conditions as discussed in Comiso (1995). Figures 9a and 9b show scatter plots of T_B(19,V) versus the difference T_B(22,V) – T_B(19,V) using SSM/I

and AMSR data, respectively. The blue data points in the scatter plot along a line OW represent data from the open ocean at all weather conditions while the black data points are those from ice covered ocean. In the open ocean, strong winds and inclement weather cause large surface waves and foam that alters the emissivity of the surface. The microwave signature of open water is thus variable and moves from low values at O, during relatively calm conditions, to higher values and towards W, in the scatter plot, depending on the strength of the disruption of the surface water. In the algorithm, these data points in blue are masked since they represent open water. The brightness temperature of open water within the ice pack corresponds to lowest values of the

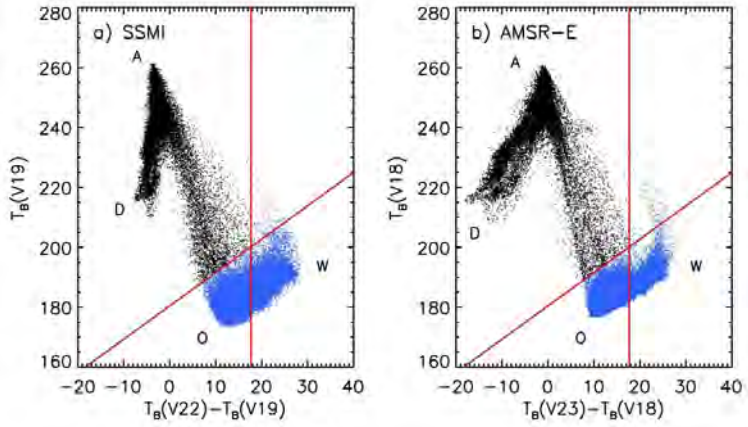

Figure 9. Scatter plots of T_B(V19, V) versus T_B(22, V) - T_B(19, V) for (a) SSM/I and (b) AMSR-E data. Data points in blue correspond to data interpreted as either ice free or <10% ice concentration.

cluster along OW since inside the pack the water surface is relatively still. The tie point used to represent T_O in equation 13 is thus a low value close to the label O (along OW). The primary mask for open water is the set of channels shown in Figures 9a and 9b. This is usually complemented by the use of the V1936 set to remove residuals. The sloping red line represents approximately 10% ice concentration and is used as a threshold. Below this threshold, ice and open ocean areas are not possible to discriminate as indicated by the data. The vertical red line is used to mask out data to the right of the line which represent primarily ice free water under abnormal or extreme surface conditions, as described in Comiso et al. (2003). We also use climatological surface temperature data or SST from AMSR2 (Shibata et al. 2010) for unusually difficult cases away from the ice pack assuming that the surface temperature of ice covered surfaces cannot have surface temperatures greater than 5 $^{\circ}$C. Because of significant variability of the emissivity of sea ice near the ice edge, the errors in the retrievals near 10% ice concentration is relatively large compared to those in high ice concentration areas. In the estimates for ice extent, which is the integral sum of the area of data elements with ice concentration greater than a certain threshold. We usually use 15% ice concentration as the threshold as was done in Zwally et al. (1983) (instead of 10%) for comparative analysis with previous estimates of extents. Other sources of systematic errors are those associated with

meltponds and new ice primarily because of unpredictable emis sivities as described in Comiso (2010).

4. Algorithm Implementation

4.1 Implementation

The discussion of the theoretical basis of the Bootstrap Algorithm in the previous section provides a general overview of the technique for estimating sea ice concentration and what it takes to obtain accurate values. To summarize, the basic equation for determining sea ice concentration is given by equation 13 while the associated technique for obtaining the key parameters needed in the determination is illustrated in Figure 7. The technique is quite simple and should provide accurate ice concentration values as long as the assumptions for obtaining the "tie-points" for 100% and 0% ice concentrations are valid. This is generally the case during dry/cold surface conditions but in the summer, the uncertainties are increased as discussed earlier.

4.2 Input/Output parameters

The input parameters are brightness temperatures as observed by AMSR2 for each data element. For ice concentration calculations, these include brightness temperatures at 18.7 GHz at vertical polarization, 36.5 GHz at both vertical and horizontal polarization, and 23.8 at vertical polarization. Input parameters include open ocean tie point, slope and offset of the regression line (red dash line in Figure 7), and thresholds for ocean mask (see Figure 9). The output is sea ice concentration.

4.3 Ancillary data

Ancillary data includes SST data as supplementary ocean mask derived from AMSR2 data and land mask derived from published land boundary data supplemented by high resolution satellite data.

4.4 Processing flow

Although only 1 set of 2 channels are required, 2 sets of channels are used by the Bootstrap Algorithm to optimize accuracy in the estimate of ice concentration: VH36 set, representing 36.5 GHz channels at both vertical and horizontal polarization and V1836 set, representing the 18.7 and 36.5 GHz channels at vertical polarization. Ice concentration is estimated using the VH36 set for data elements that are above the line AD-4K (see scatter plot in Figure 7). The ice concentration for the rest of the data elements are estimated using the V1836 set. In the process, the data element is also tested to check whether it is in land area or in the ice free open ocean area. If it is in either land or ice free ocean, ice concentration is not calculated and the data is flagged as either land or ocean.

4.5 Basic Limitations

The basic limitations of ice concentration data from AMSR2 include relatively coarse resolution and the inability to unambiguously identify areas covered by thin ice, pancake ice and meltponded ice. Thin ice, pancake ice and meltponded ice can have emissivities intermediate to those of open water and dry thick ice and could contribute to significant uncertainties in the retrieval of ice concentration. A good scheme that enables classification of each data element into different surface types would help minimize uncertainties.

5. Validation Concept

Validation of ice concentrations from AMSR2 will be done primarily using high-resolution satellite data as has been done previously (Comiso and Steffen 2001). Aircraft data from the Ice Bridge Project over both Northern and Southern Hemispheres will also be utilized for direct comparison and to validate interpretation of high-resolution satellite data. The data include detailed topography information and high resolution photos of the surface twice a year over key sea ice regions of the Arctic and the Antarctic. Special emphasis will be done on retrieved ice concentrations over new ice, marginal ice zones, and meltponded regions.

References

Bhatt, U. S., et al. 2010. Circumpolar Arctic tundra vegetation change is linked to sea-ice decline. *Earth Interactions* 14: 1-20. doi:10.1175/2010EI315.1.

Cavalieri, D. J., K. St. Germain, and C. T. Swift. 1995. Reduction of Weather Effects in the Calculation of Sea Ice Concentration with the DMSP SSM/I. *J. Glaciology* 41: 455-464.

Cavalieri, D. J., C. L. Parkinson, P. Gloersen, J. C. Comiso, and H. J. Zwally. 1999. Deriving Long-Term Time Series of Sea Ice Cover from Satellite Passive-Microwave Multisensor Data Sets. *J. Geophys. Res.* 104: 15,803-15, 814.

Cavalieri, D. J., P. Gloersen, and W. J. Campbell. 1984. Determination of sea ice parameters with the NIMBUS 7 scanning multichannel microwave radiometer. *J. Geophys. Res.* 89: 53555369.

Colbeck, S. C. 1982. An overview of seasonal snow metamorphism. *Rev. Geophys. Space Phys.* 20: 45-61.

Combes, J. M., A. Grossmann, and Ph. Tchamitchian. 1989. Wavelet: time frequency methods and phase space. In *Proceedings of the International Conference on Wavelet, Marseille, France*. New York: Springer-Verlag.

Comiso, J. C., D. J. Cavalieri, C. L. Parkinson, and P. Gloersen. 1997. Passive microwave algorithms for sea ice concentration - A comparison of two techniques. *Remote Sens. Environ.*, 60: 357-384.

Comiso, J. C. 2012. Large decadal decline in the Arctic multiyear ice cover. *J. Climate* 25(4): 1176-1193. doi: 10.1175/JCLI-D-11-00113.1.

Comiso, J. C. and F. Nishio. 2008. Trends in the sea ice cover using enhanced and compatible AMSR-E, SSM/I, and SMMR data. *J. Geophys. Res.* 113(2): C02S07. doi:10.1029/2007JC004257.

Comiso, J. C. 2009. Enhanced sea ice concentration and ice extent from AMSR-E Data. *J. Remote Sensing Soc. of Japan* 29(1): 199-215.

Comiso, J. C., D. J. Cavalieri, and T. Markus. 2003. Sea ice concentration, ice temperature, and snow depth, using AMSR-E data. *IEEE TGRS* 41(2): 243-252.

Comiso, J. C. 2010. *Polar Oceans from Space*. New York: Springerverlag.

Comiso, J. C. 1986. Characteristics of winter sea ice from satellite multispectral microwave observations. *J. Geophys. Rev.* 91(C1): 975-994.

Comiso, J. C. and K. Steffen. 2001. Studies of Antarctic sea ice concentrations from satellite data and their applications. *J. Geophys. Res.* 106(C12): 31361-31385.

Comiso, J. C. and C. L. Parkinson. 2008. Arctic sea ice parameters from AMSR-E using two techniques, and comparisons with sea ice from SSM/I. *J. Geophys. Res.* 113(C2): C02S05. doi:10.1029/2007JC004255.

Comiso, J. C. 1995. *SSM/I Concentrations using the Bootstrap Algorithm*. NASA RP 1380. Goddard Space Flight Center: National Aeronautics and Space Administration.

Fraser R. S., N. E. Gaut, E. C. Reifenstein, and H. Sievering. 1975. Interaction Mechanisms--Within the Atmosphere. In *Manual of Remote Sensing* edited by R. G. Reeves, A. Anson, D. Landen, 181-223. Falls Church, VA: American Society of Photogrammetry.

Gloersen, P. and D. J. Cavalieri. 1986. Reduction of weather effects in the calculation of sea ice concentration from microwave radiances. *J. Geophys. Res.* 91: 3913-3919.

Kelly, R. E. J, A. T. C. Chang, L. Tsang, and J. L. Foster. 2003. A prototype AMSR-E global snow area and snow depth algorithm. *IEEE Transactions on Geoscience and Remote Sensing* 41(2): 230-242.

Kummerow, C. 1993. On the accuracy of the Eddington approximation for radiative transfer in the microwave frequencies. *J. Geophys. Res.* 98: 2757-2765.

Lindsay, R. W. and J. Zhang. 2005. The thinning of Arctic sea ice , 1988-2003: Have we reached the tipping point? *J. Climate* 18: 4879-4894.

Liu, A. K. and D. J. Cavalieri. 1998. On sea ice drift from the wavelet analysis of the Defense Meteorological Satellite Program (DMSP) Special Sensor Microwave Imager (SSM/I) data. *Int. J. Remote Sensing* 19: 1415-1423.

Markus, T. and D. J. Cavalieri. 1998. Snow depth distribution over sea ice in the Southern Ocean from satellite passive microwave data. In *Antarctic Sea Ice: Physical Processes, Interactions and Variability*, 19-39. Washington, DC: American Geophysical Union.

Markus, T. and D. J. Cavalieri. 2000. An enhancement of the NASA Team sea ice algorithm. *IEEE Trans. Geosci. and Remote Sensing* 38:1387-1398.

Markus, T. and D. J. Cavalieri. 2009. The AMSR-E NT2 sea ice concentration algorithm: its basis and implementation. *Journal of The Remote Sensing Society of Japan* 29(1): 216-225.

Markus, T. and S. T. Dokken. 2002. Evaluation of Arctic late summer passive microwave sea ice retrievals. *IEEE Trans. Geoscience Remote Sensing* 40(2): 348-356.

Matzler, C., R. O. Ramseier, and E. Svendsen. 1984. Polarization effects in sea-ice signatures. *IEEE J. Oceanic Eng.* 9: 333-338.

Parkinson, C. L. and J. C. Comiso. 2008. Antarctic sea ice from AMSR-E from two algorithms and comparisons with sea ice from SSM/I. *J. Geophys. Res.* 113(C2): C02S06. doi:10.1029/2007JC004253.

Shibata, A., H. Murakami, and J. Comiso. 2010. Anomalous Warming in the Arctic Ocean in the Summer of 2007. *J. Remote Sensing Society of Japan* 30(2): 105-113.

Sigmond, M. and J. C. Fyfe. 2010. Has the ozone hole contributed to increased Antarctic sea ice extent? *Geophys. Res. Lett.* 37(L18): L18502. doi:10.1029/2010GL044301.

Svendsen, E., C. Matzler, and T.C. Grenfell. 1987. A model for retrieving total sea ice concentration from a spaceborne dual-plarized passive microwave instrument operating near 90 GHz. *Int. J. Rem. Sens.* 8: 1479-1487.

Swift, C. T., L. S. Fedor, and R. O. Ramseier. 1985. An algorithm to measure sea ice concentration with microwave radiometers. *J. Geophys. Res.* 90(C1): 1087-1099.

Turner, J., J. C. Comiso, G. J. Marshall, T. A. Lachlan-Cope, T. Bracegirdle, T. Maksym, M. Meredith, and Z. Wang. 2009. Non-annular atmospheric circulation change induced by stratospheric ozone depletion and its role in the recent increase of Antarctic sea ice extent. *Geophy. Res. Lett.* 36(L8): L08502. doi:10.1029/2009GL037524.

Wang, M. and J. Overland. 2009. A sea ice free summer Arctic within 30 years? *Geophys. Res. Lett.* 36(L7): L07502. doi:10.1029/2009GL037820.

Yaguchi, R. and K. Cho. 2009. Validation of sea ice drift vector extraction from AMSR-E and SSM/I data using MODIS data. *J. Remote Sens. Japan* 29(1): 242-252.

Zhao, Y. and A. K. Liu. 2007. Arctic Sea-Ice Motion and Its Relation to Pressure Field. *Journal of Oceanography* 63: 505-515.

Zwally, H. J., J. C. Comiso, C. Parkinson, D. Cavalieri, P. Gloersen. 2002. Variability of the Antarctic sea ice cover. *J. Geophys. Res.* 107(C5): 1029-1047.

Zwally, H. J., J. C. Comiso, C. L. Parkinson, W. J. Campbell, F. D. Carsey, and P. Gloersen. 1983. Antarctic Sea Ice 1973-1976 from Satellite Passive Microwave Observations. *NASA Spec. Publ.* 459. Washington, DC: NASA.